



A Post-Conjunction Re-Evaluation of the Calibration and Long-term Evolution of the STEREO-A Heliospheric Imagers

S.J. Tappin¹ · C.J. Eyles^{1,2} · J.A. Davies¹

Received: 23 September 2021 / Accepted: 10 February 2022 / Published online: 17 March 2022
© The Author(s) 2022

Abstract

In two earlier articles (Tappin, Eyles and Davies in *Solar Phys.* **290**, 2143, 2015, and *Solar Phys.* **292**, 28, 2017), we used the stellar photometry to determine the calibration parameters and long-term trends of the Heliospheric Imagers (HI) on board the Solar Terrestrial Relations Observatory (STEREO). In this article we provide an update on these determinations for the ahead spacecraft (STEREO-A) to incorporate the interval after solar superior conjunction (when STEREO-B was non-operational). We describe the modifications needed to our photometry procedures to accommodate the reduced pointing stability following the switch-off of the spacecraft gyros shortly prior to conjunction. We find a small revision to the absolute levels is required. We also show that the very low rates of degradation (less than 0.2% per year) found in the earlier determinations have continued beyond solar conjunction.

Keywords Photometric calibration · Large-scale flatfield

1. Introduction

The Solar Terrestrial Relations Observatory (STEREO: Kaiser et al., 2008), launched in late 2006, is a two-spacecraft NASA mission to investigate the initiation and propagation of coronal mass ejections (CMEs) by observing them from locations separated in ecliptic longitude. The two spacecraft were placed in heliocentric orbits, one (the ahead spacecraft, STEREO-A) somewhat inside 1 AU and the other (the behind spacecraft, STEREO-B) somewhat outside. This means that the spacecraft drift ahead of and behind the Earth by approximately 22° per year.

The remote sensing capabilities of STEREO are provided by the Sun Earth Connection Coronal and Heliospheric Investigation (SECCHI: Howard et al., 2008), which is a package consisting of an EUV imager, two coronagraphs and two heliospheric imagers on each

✉ S.J. Tappin
james.tappin@stfc.ac.uk

C.J. Eyles
chris.eyles@stfc.ac.uk

J.A. Davies
jackie.davies@stfc.ac.uk

¹ RAL Space, STFC Rutherford Appleton Laboratory, Chilton, Didcot, Oxon. OX11 0QX, UK

² Laboratorio de Procesado de Imagenes, Universidad de Valencia, Valencia 46071, Spain

Table 1 Key dates in the STEREO-A timeline.

Date	Day of year	Event
12 March 2007	071	First science data
1 April 2007	091	Regular science data begins
18 September 2013	261	Start of “Pre-conjunction” analysis interval Attitude-sensing gyros turned off End of “Pre-conjunction” analysis interval
14 August 2014	227	End of science data prior to conjunction
19 May 2015	139	Superior Conjunction
1 December 2015	335	Resumption of science data following conjunction
24 February 2016	055	First pointing software upgrade
6 April 2016	097	Second pointing software upgrade
9 April 2016	100	Start of “Post-conjunction” analysis interval
20 November 2020	332	End of “Post-conjunction” analysis interval

spacecraft. The heliospheric imagers (HI; Eyles et al., 2009) use Thomson-scattered light to detect and track CMEs and other solar wind disturbances from the outer limits of the coronagraphs to 1 AU and beyond. The HI cameras have nominally circular fields of view centred on the ecliptic but offset from the Sun to the earthward side. The inner (HI-1) cameras have a field of view of 20° in diameter, centred at an elongation of 14° . While the outer (HI-2) cameras have a field diameter of 70° centred at an elongation of 53° .

STEREO-A reached a solar superior conjunction in May 2015. There was a hiatus in science data from 15 August 2014 (day 227) until 1 December 2015 (day 335), due to the loss of communications caused by the small angular separation of the spacecraft and the Sun as seen from Earth around conjunction. A summary of the key dates in the STEREO-A timeline and in this analysis is given in Table 1. After the conjunction, science data resumed with the spacecraft rolled by 180° about the spacecraft-Sun direction to allow the high-gain antenna to be directed toward Earth (this also maintained the HI fields of view to the Earthward side of the Sun).

Contact with STEREO-B was lost on 1 October 2014 (day 274) during preparations for solar conjunction operations, and attempts to re-establish communication were not successful (and were abandoned in 2018).

In two earlier articles (Tappin, Eyles, and Davies, 2015, 2017) we used stellar photometry to analyse the calibration and evolution of the HI-2 and HI-1 heliospheric imagers, respectively. That analysis covered the interval from the start of regular scientific observations up to shortly before the conjunction. Since those studies, about five years of data from STEREO-A have been collected. Here we extend that analysis for STEREO-A to include those data.

In the next section we consider the implications of the switching-off of the attitude sensing gyros that took place shortly before conjunction. Since the resultant degradation of pointing stability forces us to use the daily single-exposure data for the post-conjunction analysis, in Section 3 we reanalyse the gyro-stabilized data to establish consistency between the single-exposure and science datasets, and also make a re-assessment of the absolute sensitivity. In Section 4 we extend the analysis to the post-conjunction data and determine the long-term trends in gain. We then combine the results of both analyses to produce absolute calibration parameters for the mission up to late 2020 (Section 5).

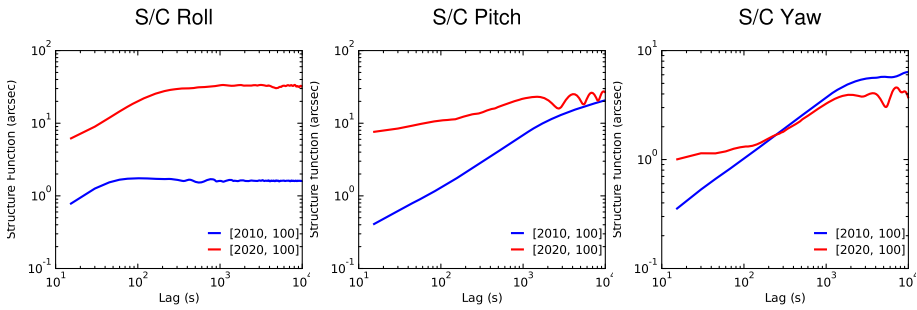


Figure 1 Structure functions of the STEREO-A pointing stability about each of the three spacecraft axes for two 48-hour intervals, starting on 10 April 2010 ([2010, 100], blue traces, gyro controlled) and 9 April 2020 ([2020, 100], red traces, no gyros).

We also include an appendix in which we show that the effects considered in this article do not have any significant influence on the calibration of HI-2B as presented by Tappin, Eyles, and Davies (2015).

2. Observations with Gyroless Attitude Control

As was noted by Tappin, Eyles, and Davies (2017), the gyros used for attitude sensing on STEREO-A were turned off during normal observations on 18 September 2013 (day 261) to conserve their remaining lifetime for necessary spacecraft calibration rolls, as they were showing signs of wear. The resulting degradation of pointing control was immediately apparent as a drop in the apparent gain of HI-1. This was caused by the sub-pixel shifts in the position of the stars between successive exposures, which cause small but significant changes in the count rate in individual pixels. This leads to the flagging of parts of the stellar signal by the particle hit scrubbing algorithm (see Figure 3 of Tappin, Eyles, and Davies, 2017). This effect has been analysed in some detail by Tappin (2017).

Following the return to full operations after the conjunction interval, improved spacecraft pointing control algorithms were developed and implemented on 24 February 2016 (day 55), and on 6 April 2016 (day 97). While the second update is reflected in a significant improvement in spacecraft pointing stability compared with early gyroless observations, and consequently in measured gain, the degradation is still apparent when compared with the observations where the gyros were still in use. This is seen in the structure functions (essentially the RMS pointing shift at a given lag) of the spacecraft pointing (Figure 1). We define the structure function as:

$$S(f; L) = \sqrt{\frac{\sum_{i=0}^{N-L-1} (f_i - f_{i+L})^2}{N - L}}, \tag{1}$$

where f is the time series to be analysed, f_i is an individual measurement and L is the lag (in samples). It is also apparent from the upper rows of Figure 2, where the normalized gain trends for the science data are plotted for both imagers (see Tappin, Eyles, and Davies, 2015, 2017 and Section 4.1 for an explanation of the normalization process).

Since the performance from the start of gyroless operations up to the start of April 2016 was markedly worse than for more recent data, that interval has been excluded from the

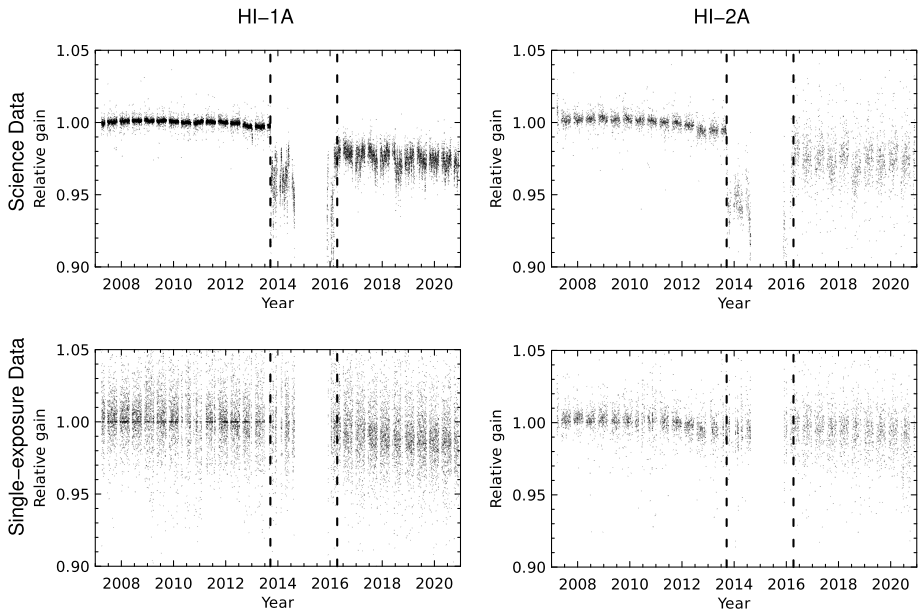


Figure 2 Trends of the gain of the HI-1A and HI-2A instruments over the STEREO mission. The data points show the median count rate of each star for each transit of the inner 200 bin radius of the field, normalized to the median rate for that star over the interval from 1 April 2007 (day 91) to 17 September 2013 (day 260). The vertical dashed lines indicate the times at which the gyros were disabled, and at which the improved gyroless control was implemented. In the case of the HI-2A single-exposure data, the images were binned before photometry (see Section 3.2.2, for an explanation).

analysis presented in this article. For convenience, we refer to the interval from the start of routine science data up to the gyro switch off (1 April 2007 (day 91) to 17 September 2013 (day 260)) as the pre-conjunction interval, and the interval from the pointing upgrade to the last data used (9 April 2016 (day 100) to 27 November 2020 (day 332)) as the post-conjunction interval.

The regular science images for both HI-1 and HI-2 are generated by binning the 2048×2048 pixel CCD output to 1024×1024 bins and summing over 30 exposures for HI-1 and 99 exposures for HI-2. One such science image is generated by HI-1 every 40 minutes and every two hours for HI-2. Details of the processing are given in Eyles et al. (2009). However, in addition one full-resolution (2048×2048) single-exposure image from each imager is downlinked each day. The on-board particle scrubbing is not applied to these, so they should not be affected by the pointing degradation. This advantage is however countered by the fact that the total integration per day is much less than for the science data, only 40 seconds vs. 12 hours for HI-1 and 50 seconds vs. 16.5 hours for HI-2. There is also a small chance that particle hits contaminating the count rate measurements during solar energetic particle (SEP) events, but given the low hit rate in single exposures at other times, this is not a significant effect. The apparent gain changes for these data are shown in the lower rows of Figure 2. From this overview it is evident that there is no clear discontinuity in apparent gain at the switch to gyroless operations for the single exposure data, whereas for the science data there is a definite drop. It is also clear that the scatter in the gain determinations across the entire mission is clearly greater for the single-exposure data, this is particularly evident in HI-1A.

3. Comparison with Earlier Determinations

Since the use of single exposures has some implications for the choice of the stellar sample and for the photometry, we must first compare the results from the science and single-exposure datasets in the interval during which the gyros were operating, and also with the results from our previous analyses that used only science images (Tappin, Eyles, and Davies, 2015, 2017).

3.1. HI-1A

3.1.1. Stellar Sample and Photometry

For the analysis of HI-1 presented in Tappin, Eyles, and Davies (2017) we used a stellar sample from the SKY2000 catalogue (Myers et al., 2001), and we use the same source in this analysis. In common with the earlier analysis, we restrict our attention to measurements within 200 bins (400 pixels) of the centre of the field of view. So as to have a common sample suitable for both science and single exposure data, and both before and after conjunction, the selection criteria are similar but not identical to those used by Tappin, Eyles, and Davies (2017). The environmental and spectral criteria follow those of Tappin, Eyles, and Davies (2017), i.e.:

- The star must not be a double one (whether binary or optical).
- It must not be listed as variable.
- It must not lie within 0.2° of another star in the catalogue (i.e. a star brighter than magnitude 10.0).
- It must not have a peculiar or variable spectral type.
- It must have a spectral type that can be matched to a spectrum in Pickles' collection of stellar spectra (Pickles, 1998a). A spectral match is considered valid if: the luminosity class is a single value (e.g. stars with luminosity class III-IV would be rejected as Pickles (1998a) has no spectra for such cases), and one of the following is satisfied:
 - i) There is an exact match to a type with a spectrum.
 - ii) The spectral type lies within a range that shares a common spectrum in the Pickles' (1998a) catalogue (e.g. Pickles, 1998a lists a single spectrum for B1-2III stars that would be used for both B1III and B2III).
 - iii) The spectral type is a range that spans a spectrum in Pickles (1998a) (e.g. a star listed as G8-K0III could match any of G8III, G9III or K0III)
 - iv) The spectral type can be matched by interpolating between two spectra separated by no more than three subclasses (e.g. K4 could be derived from K2 and K5, but not from K2 and K6).

In all cases, an exact luminosity class match is required (e.g. we would not attempt to interpolate between A2I and A2III to obtain a spectrum for A2II; we do however consider the supergiant classes I, Ia, and Ib to be equivalent). Unlike the analysis in Bewsher et al. (2010) and Bewsher, Brown, and Eyles (2012), it was not necessary to resort to colour mixing as spectral types were available for all of the stars in our sample and the vast majority could be matched to spectra in Pickles (1998a); those few that could not be adequately matched to a spectrum in Pickles (1998a) were discarded.

A number of other criteria, though similar, were modified to streamline the process, or by applying thresholds that were imposed in a post-selection winnowing by Tappin, Eyles, and Davies (2017):

Table 2 Sample selection criteria for HI-1.

Parameter	Unit	Pre-conjunction		Post-conjunction	
		Science	Single	Science	Single
Min. observations		400	15	300	12
Min. ratio				0.75	
Max. ratio				1.5	
Max. IQ range	fractional	0.03	0.1	0.03	0.1
Max. position error	CCD pixels			0.6	
Max. background	DN s ⁻¹			0.2	
Max. count rate	DN s ⁻¹			1000.0	
Faintest magnitude				9.0	
Closest neighbour	°			0.2	
Min. galactic lat.	°			15.0	

- The stars must not be fainter than a photonic magnitude of 9.0 (0.5 magnitudes fainter than Tappin, Eyles, and Davies, 2017).
- Rather than imposing a bright magnitude limit and a count rate limit we apply only a count rate limit of 1000 DN s⁻¹ (c.f. 400 DN s⁻¹ in Tappin, Eyles, and Davies, 2017), as we now think that the earlier limit was overly conservative and driven by an incomplete understanding of the effects of particle scrubbing.
- We also reject stars that have median count rates less than 0.75 or more than 1.5 times the rates predicted, in any of the observation series (science and single exposure data, pre-conjunction and post-conjunction intervals).
- Stars below 15° galactic latitude were also excluded.
- Stars with an average position more than 0.3 bins or 0.6 pixels from the calculated position are considered to be possible misidentifications, and so were excluded.
- Stars with a high background count rate (more than 0.2 DN s⁻¹) were also excluded.

Finally, a number of criteria must have different thresholds for the different datasets:

- The number of observations required differs between the datasets as the sampling and the duration of the datasets differ.
- Different thresholds are needed for the interquartile (IQ) range as the typical scatter ranges for a star vary significantly between the datasets.

To be used in any analysis, the stars must be suitable for use in all of the datasets. The quantitative criteria are summarized in Table 2. In addition to the criteria thus defined, two stars were excluded manually as having anomalous behaviour, leaving a total of 1391 stars for the analysis.

Since the single-exposures are 2048 pixel square images rather than 1024 bin square images, it is necessary to analyse the curve of growth for the photometry apertures to determine the optimal apertures for the single-exposure data. The testing followed the pattern used by Tappin, Eyles, and Davies (2017), with the addition of a group of smaller apertures (less than two pixels), thus a common background annulus is used for a range of aperture radii, and the largest radius of any set is repeated with the next larger set as well. The aperture ranges used along with the associated background annuli are listed in Table 3, and the results are shown in Figure 3.

While the form of the curve is similar to that found for the science data, there are two noticeable differences:

Table 3 Summary of the aperture ranges and background annuli used to determine the aperture photometry curves of the growth shown in Figure 3, all values are in CCD pixels.

Group	Min radius	Max radius	Radius step	Background	
				Inner radius	Outer radius
0	1.2	2.4	0.2	4.0	8.0
1	2.4	6.0	0.4	8.0	16.0
2	6.0	10.0	0.4	12.0	20.0
3	10.0	14.0	0.4	16.0	24.0
4	14.0	24.0	1.0	26.0	32.0

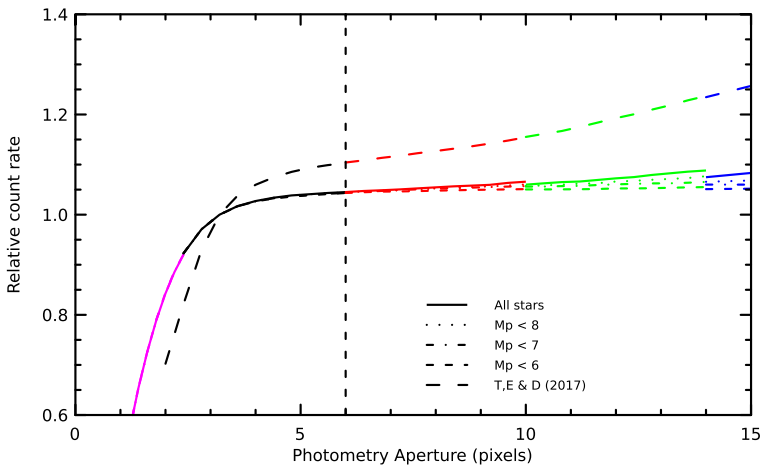


Figure 3 Aperture photometry curves of growth for HI-1A single exposure images out to a photometry radius of 15 pixels, determined over the interval from 30 May 2007 (day 150) to 30 May 2009. The “all stars” curve from the science data of Tappin, Eyles, and Davies (2017) is also shown as the long dashed line (aperture rescaled to pixels). The vertical dashed line indicates the aperture of 3.0 bins used by Tappin, Eyles, and Davies (2017). The colours of the lines separate the groups as outlined in Table 3. Apertures above 15 pixels are not shown to allow the flat region of the curve to be more clearly seen.

- i) The growth of the measured signal for large apertures is significantly slower, this means that the aperture selection is less critical than for the science data.
- ii) The discontinuities between the measurement groups are more evident. This appears to indicate that the background determination in the stellar photometry is somewhat more affected by the size of the background annulus for the single exposure data than for the science data, it is however only evident at apertures and annuli larger than those used in the final analyses.

Since the levels are normalized to a value of 1.0 at 3.2 pixels (1.6 bins, which was the normalization size used by Tappin, Eyles, and Davies, 2017), a direct comparison of the levels is not possible. Given the similarity of form, we think it is most sensible to simply use the same physical radii as for the science data (where we follow Tappin, Eyles, and Davies (2017) in using an aperture of 3.0 bins and a background annulus from 5.0 to 10.0 bins), i.e. an aperture of 6.0 pixels and a background annulus from 10.0 to 20.0 pixels.

Table 4 Median gains and constrained fits (as in Tappin, Eyles, and Davies, 2017) from HI-1A data from the pre-conjunction analysis interval.

Sample	N_{stars}	Simple median		Constrained fit	
		Gain	Error	Gain	Error
Science	1391	0.934	0.007	0.916	0.02
Single	1391	0.939	0.008	0.931	0.02
Tappin, Eyles, and Davies (2017)	1422			0.918	0.008
Tappin, Eyles, and Davies (2017) reanalysed	1334	0.932	0.008	0.911	0.02
Bewsher et al. (2010)				0.93	

A significant difference in the analysis is in the method of fitting. We now consider that the best method to determine the levels is simply to compute the median of the ratio of measured to computed count rates for all individual stellar measurements, thus minimizing potential biasing through grouping the measurements by star prior to fitting. In Tappin, Eyles, and Davies (2017) (and also in Tappin, Eyles, and Davies, 2015) we took a median ratio for each star and then performed a fit constrained to pass through the origin, weighting each star in the fit by the number of observations of that star.

Measurements for all images prior to 17 September 2013 (day 260) were analysed. In addition to the sample selection, we rejected any individual measurements:

- where a star's measured count rate was more than twice or less than half of its median count rate in the interval, or
- where its position was more than 1.5 bins (for the science data) or 2.0 pixels (for the single-exposure data) away from the expected location

as a probable bad measurement, i.e. the location algorithm had converged on the wrong star or that the measurement was contaminated (e.g. by a planet or a particle hit).

As discussed by Tappin, Eyles, and Davies (2017) and Tappin (2017), the particle scrubbing causes some erosion of the measured stellar count rates because of the motion of the stars due to the orbital motion of the spacecraft. To compensate for this, all of the measured count rates from the science datasets were corrected using the recipe given in Tappin, Eyles, and Davies (2017):

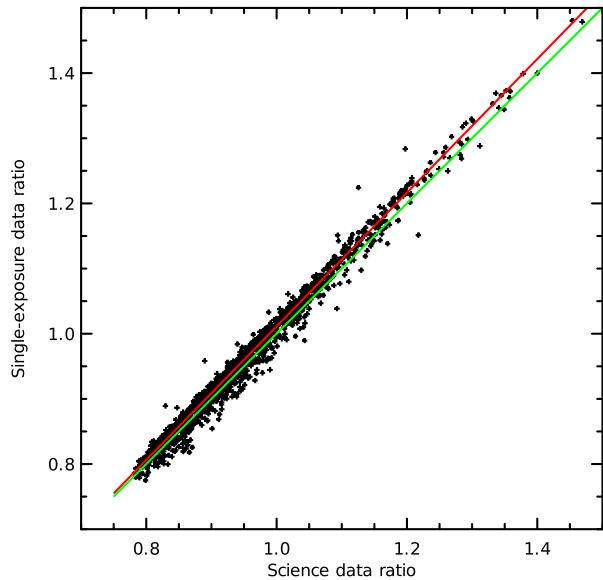
$$\frac{R_{\text{scrubbed}}}{R_{\text{unscrubbed}}} = \left\{ \begin{array}{l} 0.981 + 0.0013 m_v \\ 0.933 + 0.0071 m_v \\ 0.989 \end{array} \right\} \text{ where } \left\{ \begin{array}{l} 7.5 \leq m_v < 9.0 \\ 5.0 \leq m_v < 7.5 \\ m_v < 5.0 \end{array} \right. , \quad (2)$$

where R_{scrubbed} is the actual measured count rate and $R_{\text{unscrubbed}}$ is the required corrected rate. Since there is no on board scrubbing in the single exposure dataset, no such correction is needed.

3.1.2. Results

In Table 4 we show the results obtained for both the science and single exposure gyro-stabilized datasets and also for the stellar sample used by Tappin, Eyles, and Davies (2017), both the original analysis and also a reanalysis using the star list from Tappin, Eyles, and Davies (2017), but with re-measured count rates and analysed using the methods of this study (we cannot use the same star list as Tappin, Eyles, and Davies (2017) for the main

Figure 4 Comparison of the ratios of measured to calculated count rates for HI-1A for science and single-exposure data, in the pre-conjunction interval. The science rates are corrected by the factors determined by Equation 2. The red line shows the L1-norm fit from Equation 4, and the green line shows the case of equality.



study, as a small number of the stars is unsuitable either post-conjunction or in the single exposure data). We have computed both the simple median and also the constrained fit (as used by Tappin, Eyles, and Davies, 2017). All errors are computed following the recipe of Koenker and Hallock (2001) as

$$E(x) = \frac{\text{fr}\left(x, \frac{1}{2} + \frac{1}{\sqrt{N}}\right) - \text{fr}\left(x, \frac{1}{2} - \frac{1}{\sqrt{N}}\right)}{2}, \tag{3}$$

where $\text{fr}(x, f)$ represents the f th fractile of x , and N is the number of observations. Since the variation between stars is much greater than that within the series of any individual star, we regard the number of observations as being the number of stars used rather than the total number of individual measurements.

It is evident that while the gains calculated from the science and single exposure datasets using the simple median method are in good agreement with each other, they are somewhat out of agreement with the published values of Tappin, Eyles, and Davies (2017). It is also clear that when we apply the constrained fit method to the current science dataset, the results agree within the errors with the analysis of Tappin, Eyles, and Davies (2017), and equally applying the simple median ratio to the Tappin, Eyles, and Davies (2017) stellar sample gives values that agree with the newer determination. For the single exposure data however, there is little difference between the simple median and the constrained fit. This value is also close to the value found by Bewsher et al. (2010).

We also find that there is an excellent correlation between the median ratio for each individual star in the science and single-exposure datasets (Figure 4). The fitted trend using an L1-norm fit is:

$$R_{\text{single-exposure}} = -0.01429 + 1.0256 R_{\text{science}}, \tag{4}$$

with a Spearman rank correlation coefficient of 0.989.

Table 5 Sample selection criteria for HI-2. The parameters are as described in Table 2.

Parameter	Unit	Pre-conjunction		Post-conjunction	
		Science	Single	Science	Single
Min. Observations		600	20	400	20
Min. ratio				0.75	
Max. ratio				1.5	
Max. IQ range	fractional			0.1	
Max. position error	CCD pixel			1.0	
Max. background	DN s ⁻¹	50.0	100.0	50.0	100.0
Max. count rate	DN s ⁻¹			2500.0	
Faintest magnitude				7.5	
Closest neighbour	°			0.5	
Min. Galactic Lat.	°			15.0	

In summary, we find that for HI-1A, the single exposure images give an instrument gain consistent with that obtained from the science images. But we do find a discrepancy of about 2% with our previously published values (Tappin, Eyles, and Davies, 2017). This discrepancy appears to be related to the method used to determine the level rather than any bias from the differences between the stellar samples.

3.2. HI-2A

3.2.1. Stellar Sample and Photometry

In the original HI-2 calibrations (Tappin, Eyles, and Davies, 2015), a relatively small sample of stars was chosen. While such a sample is suitable for use with the science data, we considered it unlikely to be large enough to give adequate statistics with the single exposure data (and certainly an analysis using a larger sample is needed to verify this).

The Tappin, Eyles, and Davies (2015) sample was selected from the Yale Bright Star list (Hoffleit and Warren, 1995) that only extends to magnitude 6.5. So to get a larger sample, it is necessary to use a deeper catalogue. Since we are already using it for HI-1, the obvious choice is to use the SKY2000 catalogue (Myers et al., 2001).

The new baseline sample is defined to include stars that pass within 200 bins of the centre of the HI-2A field of view (for consistency with the HI-1 analyses) and:

- Have a visual (V) magnitude brighter than 7.5.
- Have a well-defined spectral type that can be matched to a spectrum in the spectral atlas of Pickles (1998a,b). See Section 3.1.1 above and also Tappin, Eyles, and Davies (2015) for the rules for matching spectra.
- Do not have any form of “anomalous” spectrum.
- Are not classified as variables.
- Any neighbouring star within 0.5° must be more than 2.0 magnitudes fainter than the star being measured.

The main differences from the sample used by Tappin, Eyles, and Davies (2015) are the fainter magnitude limit and the fact that we have expanded the analysis region from 100 bins to 200 bins.

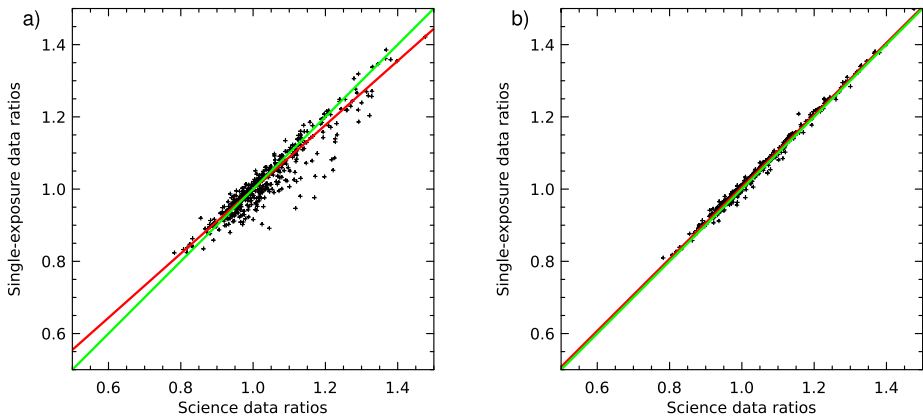


Figure 5 Correlation of the HI-2A science and single-exposure gain ratios. **(a)** Single-exposure photometry on unbinned data. **(b)** Single-exposure photometry on 2×2 binned data. The red lines show the regression of the datasets, the green lines show the ideal case of equality.

The count rates for all stars were measured for all available images using the “descents” photometry method described by Tappin, Eyles, and Davies (2015). In essence this selects the region surrounding the peak over which the measured count rate is decreasing away from the peak, this method was found to yield more consistent count rates for HI-2 than the aperture photometry method as it handles the highly variable point spread function better.

For the detailed analysis, further selections are then made in a similar manner to that used for HI-1A, however the actual threshold criteria differ. These are listed in Table 5. This leaves a final analysis sample of 448 stars (compared with only 62, within 100 bins of the field centre, in Tappin, Eyles, and Davies, 2015). It should be noted that owing to the different photometry methods, the background levels are not comparable.

In addition, as with HI-1A, we excluded individual measurements that were outside the range of 0.5 to 2.0 times the median count rate for the star, and ones where the measured position was more than 1.5 bins for science data or more than 2.0 pixels for single exposure data away from the expected location.

3.2.2. Results

When comparing the ratio of the median count rates to the predicted values for HI-2A in the pre-conjunction interval, it became clear that some stars were systematically lower in the unbinned single-exposure data than in the science data (Figure 5a), while others were close to the expected trend. This is confirmed by a regression that yields a fit of:

$$R_{\text{single-exposure}} = 0.11030 + 0.8892 R_{\text{science}}, \tag{5}$$

with a Spearman rank correlation of only 0.922. One plausible contributor to this is that the lower signal-to-noise ratio of the single-exposure images results in some premature termination of the descents. As a check on this, we re-ran the photometry using single-exposure data rebinned to 1024 by 1024 (i.e. the same resolution as the science data), this yields the trend in Figure 5b and a regression of:

$$R_{\text{single-exposure}} = 0.00965 + 0.9966 R_{\text{science}}, \tag{6}$$

Table 6 Median gains for HI-2A in the pre-conjunction analysis interval.

Sample	N_{stars}	Simple median		Constrained fit	
		Gain	Error	Gain	Error
Science	443	1.005	0.01	1.003	0.02
Science (R=100)	229	0.992	0.015	0.988	0.03
Science ($m_v < 6$)	115	0.975	0.015	0.976	0.03
Science ($m_v < 6$, R=100)	61	0.958	0.015	0.954	0.03
Single (unbinned)	443	0.996	0.01	0.990	0.017
Single (binned)	443	1.009	0.01	1.007	0.02
Single (100, unbinned)	229	0.983	0.015	0.978	0.024
Single (100, binned)	229	0.996	0.015	0.990	0.025
Tappin, Eyles, and Davies (2015)	62			0.959	0.02
Tappin, Eyles, and Davies (2015) reanalysed	97	0.976	0.02	0.978	0.02

with a Spearman correlation of 0.994, confirming our hypothesis. The excellent correspondence between the datasets in the binned case shows that the binned single-exposure data give good photometric performance with the descents method.

A summary of the fitted gains for HI-2 is given in Table 6. We see that the gains computed here are somewhat higher than those previously determined by Tappin, Eyles, and Davies (2015). Unlike in the case of HI-1, there is no clear difference between the median and constrained fit methods. There are however several trends:

- Science data measurements using only stars brighter than $m_v = 6$ show a lower apparent gain than those using stars down to $m_v = 7.5$. Very similar values are also obtained using the sample from Tappin, Eyles, and Davies (2015) (which went to $m_v = 6.5$ but was far from complete for magnitudes fainter than 6.0) and applying the current analysis methods.
- Science data measurements using only the central 100 bin region of the CCD show a lower apparent gain than those using the central 200 bin region.
- Single-exposure measurements where the data were binned before the photometry show a higher apparent gain than those where the photometry was done on the raw images, and a much closer match to the results from the science data. We will therefore use the photometry from binned data for HI-2A single-exposure images hereafter.

When we examine the histograms of the ratio of the measured to computed count rates (Figure 6) it becomes clear that in the datasets using only bright stars there is a deficit of high ratios $\frac{R_{meas}}{R_{comp}} > 1.2$, this is particularly apparent in the case of the inner core bright dataset ($R = 100$, $m_v < 6$). It should be noted that the difference between the inner 100 bin and the inner 200 bin determination is in the opposite sense from that expected if the instrument flat field correction had not been applied.

The differences between the single-exposure and science data medians are comparatively small (of the order of 1%), and the histograms (Figure 7) show that the distributions are very similar.

3.3. Summary

While it is clear that the single-exposure datasets do not provide as good a measure of instrument performance as the science data, mainly owing to the much lower total integra-

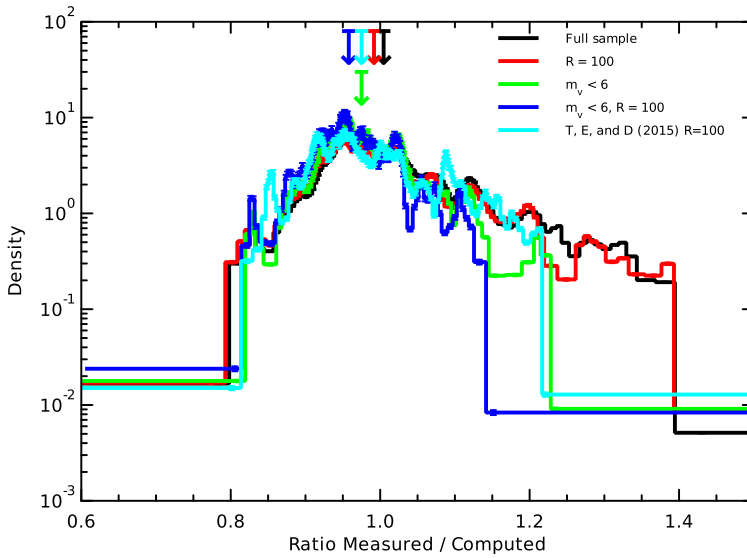


Figure 6 Histogram of the ratio of measured to predicted count rates for a number of HI-2 science-data analysis samples (as in Table 6). The histogram for the Tappin, Eyles, and Davies (2015) sample is from the reanalysed dataset. These histograms have a constant number of measurements per bin, and are normalized to the total number of measurements in the sample. The error bars are the errors derived from Poisson counting statistics, and are placed at the median ratio of the measurements in the bins. The arrows above the plot traces show the medians of each distribution.

tion time, they do give a sufficiently reliable measure to allow their use to analyse the performance trends in the post-conjunction epoch, when degraded pointing stability resulting from the gyroless operation prevents the use of science images for calibration. For HI-2A, the results are significantly improved by 2×2 binning the single-exposure data before photometry.

We also note that for most stars the ratio of measured to predicted count rate is very similar in the two datasets.

Finally, we see that for HI-2A, there is a need to revise the gain upward compared with the values determined by Tappin, Eyles, and Davies (2015).

4. Determination of the Performance Trends Since Conjunction

4.1. Overview

We have already seen (Tappin, Eyles, and Davies, 2015, 2017) that the spread of the measurements of the ratio of the count rate to that computed from the pre-launch modelling is too large to allow the determination of a trend in the gains, and also that this spread is dominated by the variation from star to star, rather than the variation of the measurements of individual stars.

A solution to this problem is to normalize the values for each star to the median value for that star over the determination interval and then determine a relative variation. This was the method used by Tappin, Eyles, and Davies (2015, 2017), and also used here.

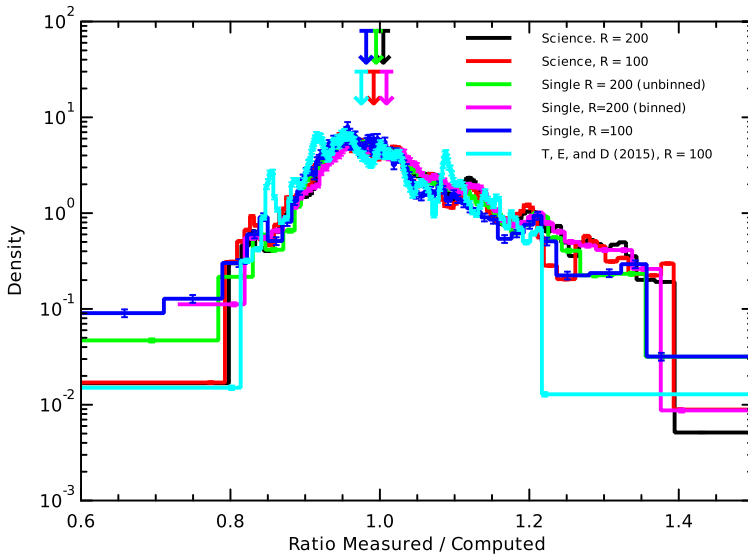


Figure 7 Histograms of the ratio of measured to predicted count rates comparing the science and single-exposure datasets. The format is the same as for Figure 6.

For this approach to be considered valid across the entire mission, we must verify that consistency is maintained in the post-conjunction interval where the stars are crossing a different region of the CCD because of the 180° roll of the spacecraft. To do this, we compared the ratios of median measured to calculated count rates for all of the stars used in the samples for both science and binned single-exposure data for the pre-conjunction interval (1 April 2007 to 17 September 2013) with those for the post-conjunction interval (9 April 2016 to 27 November 2020). These trends are shown in Figure 8. From these it is very clear that the behaviour of the individual stars is highly consistent across the entire interval of study. As expected from the degraded pointing leading to increased false positives in the particle scrubbing (Tappin, 2017), the fits to the science data show lower count rates in the post-conjunction interval than in the pre-conjunction interval, whereas the single-exposure data count rates are very similar for the two intervals.

We also did analyses similar to those above, but separating into stars at northern and southern ecliptic latitudes. We did not find any significant differences in any dataset. This confirms that there is no detectable effect from the 180° spacecraft roll following conjunction.

For consistency, we have chosen to use the pre-conjunction interval as the baseline for normalizing all of the datasets, i.e.:

$$R_{\text{Norm}} = \frac{R}{\text{median}(R(2007 : 91, 2013 : 260))}, \tag{7}$$

where $\text{median}(R(2007 : 91, 2013 : 260))$ is the median count rate over the interval from day 91 (1 April) 2007 to day 260 (17 September) 2013.

In all cases, the fitting of trends uses an L1-norm fit to the individual measurements. For convenience, fits are calculated based on time in Julian years (365.25 days) after 2007.0.

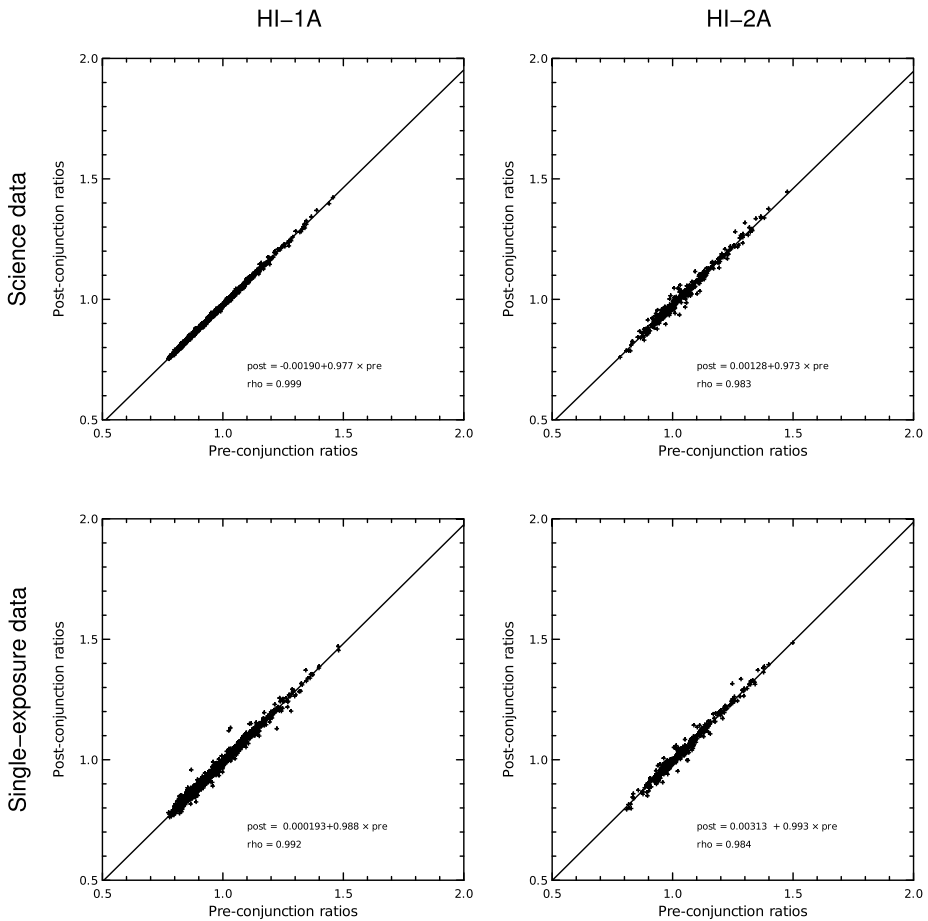


Figure 8 Comparison of pre-conjunction (1 April 2007 to 17 September 2013) and post-conjunction (9 April 2016 to 27 November 2020) count rate ratios for the various STEREO-A HI datasets. Each symbol represents one star. N.B. The correction for particle scrubbing (Equation 2) has not been applied to the HI-1A science data as the factor would be the same for both datasets. The fit and Spearman rank correlation (ρ) are added to each plot.

4.2. HI-1A

From Figure 2, several features of the trends in normalized count rates are apparent:

- There is a visible reduction of gain in the post-conjunction interval (after the second vertical dashed line) compared with the pre-conjunction interval (before the first vertical line), even in the single-exposure data.
- The single-exposure data have a much wider spread than the science data, both pre- and post-conjunction. Although relative to counting statistics, the scatter is less for the single-exposure data (3–5 times counting vs. 5–8 times for science data).
- The interval of comparatively poor pointing control (between the two dashed lines) is not clearly visible in the single-exposure data (Figure 2), whereas it appears as a significant drop in apparent gain in the science data.

- In the science dataset there is at least a hint of a maximum in the gain in the early part of the mission. This was noted by Tappin, Eyles, and Davies (2017) and treated as a constant gain up to the start of 2009.

For fitting, we used three intervals: the pre-conjunction interval, the post-conjunction interval, and both together. For each interval and dataset, we fit:

$$R_{\text{Norm}}(T) = R_0 + R_1 T, \quad (8)$$

where T is the time in years after 2007.0. For the pre-conjunction interval and the combined interval, we also did a quadratic fit:

$$R_{\text{Norm}}^{(q)}(T) = R_0^{(q)} + R_1^{(q)} T + R_2^{(q)} T^2. \quad (9)$$

For those two intervals, we also used a linear fit with a break:

$$R_{\text{Norm}}^{(b)}(T) = R_0^{(b)} + R_1^{(b)} \max(T, T_b). \quad (10)$$

This is similar to the fit using a constant level prior to 2009.0, and a linear fit thereafter, as used by Tappin, Eyles, and Davies (2017). However, here the end of the constant interval (T_b) is a free parameter, whereas in the analysis of Tappin, Eyles, and Davies (2017), the break at 2009.0 was estimated rather than fitted.

The fits are shown in Table 7. Note that since these are fits to normalized data, the constant term only reflects the change between the level at the fitting origin (2007.0) and the mean level over the normalization interval. A number of general points may be gleaned from the tabulated fits:

- All show only minor loss of sensitivity over the entire mission to date.
- All of the quadratic fits show a positive linear term and negative second-order term, giving a maximum (see Table 7 for the dates) during the pre-conjunction interval.
- The post-conjunction linear fits have similar gradients for both science and single-exposure data, but with a significant offset between them.
- The linear fits with a break all show the break occurring in mid to late 2011, compared with 2009.0 used by Tappin, Eyles, and Davies (2017), which was an estimate and not a fitted parameter.

The various fits to the pre-conjunction data are shown in Figure 9, along with the previous published trend and also the linear fit to the single-exposure data from the post-conjunction interval. As might be expected, the fits do not differ by more than about 0.5% over the pre-conjunction fitting interval. However, there is considerable divergence as these fits are extended into the post-conjunction epoch, with the different methods differing more than the different datasets. Comparison of the various pre-conjunction fits with the post-conjunction linear fit suggests that the linear fit with a break extrapolates to the actual behaviour in the post-conjunction interval rather better than the others.

Figure 10a compares most of the fits to the single exposure data (the quadratic fit to the pre-conjunction data is omitted for clarity). It is evident from these that the fits including post-conjunction data show a somewhat more rapid degradation than determined by Tappin, Eyles, and Davies (2017), however, the pre-conjunction linear fit with a break has a very similar slope and break point to that to all of the data. We attribute this discrepancy with the published value to having placed the break too early in the earlier (Tappin, Eyles, and Davies, 2017) analysis.

Table 7 Trend fits to the HI-1A datasets.

Linear fits (Equation 8)					
Dataset	Interval	Constant (R_0)	Linear (R_1)		
Science	Pre-conjunction	1.0018	-0.000524		
Single	Pre-conjunction	1.0010	-0.000421		
Science	Post-conjunction	0.9936	-0.001604		
Single	Post-conjunction	1.0107	-0.001976		
Science	All	1.0081	-0.002655		
Single	All	1.0033	-0.001325		
Quadratic fits (Equation 9)					
Dataset	Interval	Constant ($R_0^{(q)}$)	Linear ($R_1^{(q)}$)	Quadratic ($R_2^{(q)}$)	Maximum
Science	Pre-conjunction	0.9998	0.001117	-0.000237	2009.361
Single	Pre-conjunction	0.9996	0.000816	-0.000199	2009.046
Science	All	1.0016	0.000349	-0.000215	2007.813
Single	All	1.0003	0.000150	-0.000104	2007.717
Linear plus break fits (Equation 10)					
Dataset	Interval	Constant ($R_0^{(b)}$)	Linear ($R_1^{(b)}$)	Break (T_b)	
Science	Pre-conjunction	1.0107	-0.002146	2011.693	
Single	Pre-conjunction	1.0088	-0.001962	2011.498	
Science	All	1.0187	-0.003710	2011.876	
Single	All	1.0078	-0.001736	2011.486	

The difference between the quadratic and linear-with-break fits is very small. But it does predict a more rapid degradation towards the end of the data sample and going forward, which is not physically reasonable.

It should also be noted that the differences between all of the fits are small compared with the scatter in the individual data points, as is illustrated in Figure 10b, where the fits to all data are overlaid on the original (normalized) data.

Overall, we consider that the linear fit with a break represents the observations well and is more likely to continue to track the evolution of the performance of HI-1A than the quadratic fit, which drops off increasingly rapidly in the coming years, when we have seen no evidence of accelerating degradation beyond the initial near-constant period at the start of the mission.

4.3. HI-2A

The general trends as seen in Figure 2 are very similar to those for HI-1A, however there are a couple of additional points to note:

- The increase in scatter from the science data to the single-exposure data in the pre-conjunction interval is much less dramatic. But there is a clearer difference in the scat-

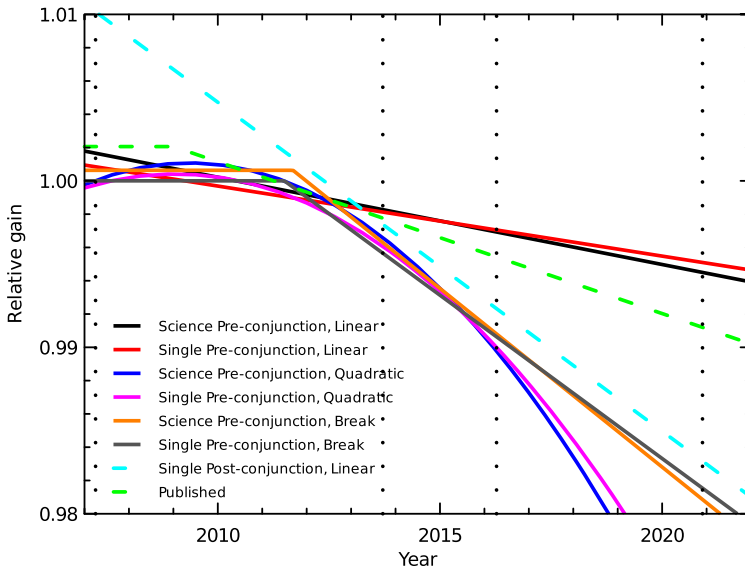


Figure 9 Comparison of the various fits to the pre-conjunction HI-1A data. In addition, the published fit from Tappin, Eyles, and Davies (2017) and a linear fit to the single-exposure post-conjunction data are included. The vertical dotted lines delimit the fitting intervals.

ter between the pre-conjunction and the post-conjunction data. For HI-2A, the single-exposure data show a scatter only about twice the counting statistics.

- There appears to be a gain increase in the single-exposure data across the conjunction interval.

As with HI-1A, we computed fits separately for the pre-conjunction, post-conjunction, and combined intervals, using the three forms from Equations 8 to 10. The results are tabulated in Table 8. A few points to note are:

- The post-conjunction fit to the science data has a significantly lower constant term than the rest of the fits. This is expected as a result of the degraded pointing and is clearly visible in Figure 2.
- The post-conjunction fit to the single-exposure data, on the other hand, has a rather higher constant term (by about 1%). This backs up the apparent performance improvement, or at least a hiatus in the decay during the conjunction interval that was seen in Figure 2. We do not have a clear explanation for this, but hypothesize a small change in some electronic component while the instrument was switched off for the conjunction.
- The quadratic terms are much smaller than was the case for HI-1A, and in the case of the fit to all of the single-exposure data the term is positive. All have maxima (or minima) outside the time span of the STEREO mission. The implication of this being that the quadratic fit is not a good model for the HI-2A data.
- The linear fits both pre- and post-conjunction correspond to degradation rates of the order of 0.1% per year.

As with HI-1A, it is instructive to plot the pre-conjunction fits (along with the linear fit to the post-conjunction singles and the published fit from Tappin, Eyles, and Davies, 2015). This is done in Figure 11. It is very apparent that the linear and quadratic fits to

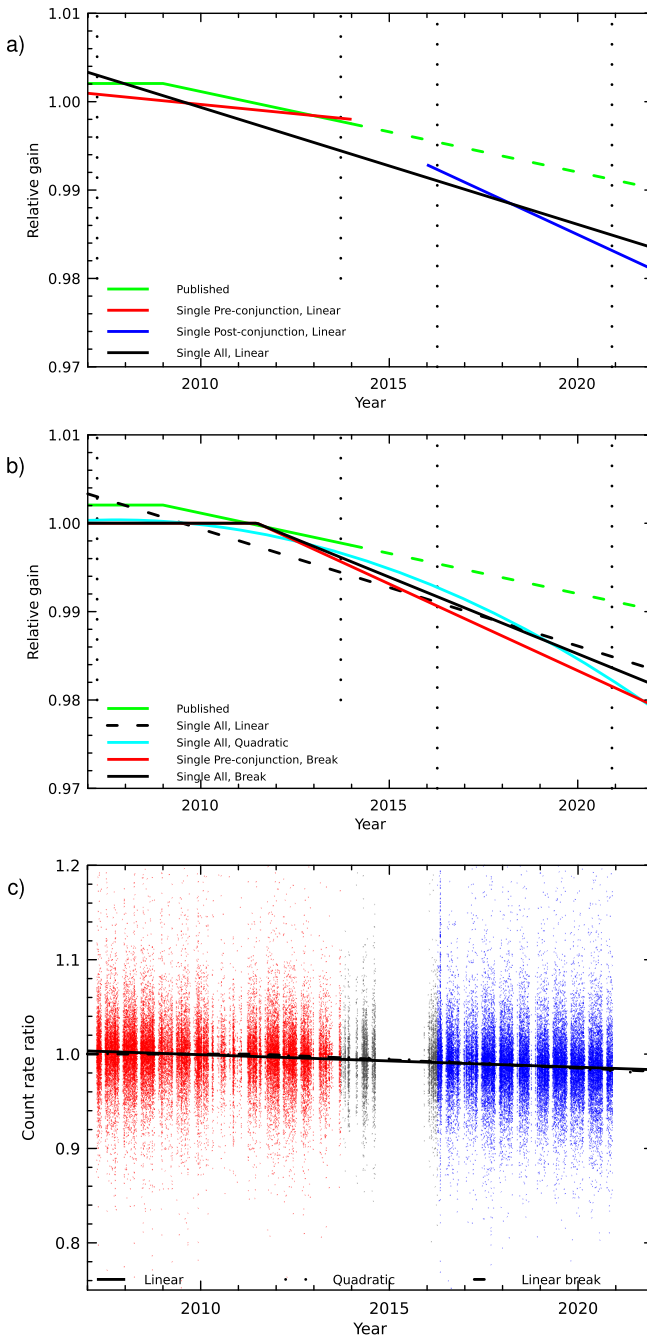


Figure 10 (a) Summary of the linear fits to single-exposure data for HI-1A. (b) Fits to all of the data along with the linear-with-break fit to the pre-conjunction interval. In both (a) and (b) the published fit of Tappin, Eyles, and Davies (2017) is shown for comparison. The vertical dotted lines mark the analysis intervals. (c) The three fits to all of the data, overlaid on the individual measurements. In (c) the red points are the pre-conjunction interval, blue the post-conjunction interval, and grey the conjunction interval which was not used in the fitting.

Table 8 Trend fits to the HI-2A datasets. In the quadratic section, parenthesized figures in the “Maximum” column indicate minima.

Linear fits (Equation 8)					
Dataset	Interval	Constant (R_0)	Linear (R_1)		
Science	Pre-conjunction	1.0047	-0.001338		
Single	Pre-conjunction	1.0039	-0.001236		
Science	Post-conjunction	0.9820	-0.000706		
Single	Post-conjunction	1.0120	-0.001594		
Science	All	1.0092	-0.002876		
Single	All	1.0029	-0.000840		
Quadratic fits (Equation 9)					
Dataset	Interval	Constant ($R_0^{(q)}$)	Linear ($R_1^{(q)}$)	Quadratic ($R_2^{(q)}$)	Maximum
Science	Pre-conjunction	1.0046	-0.001258	-1.33e-05	1959.868
Single	Pre-conjunction	1.0037	-0.001170	-6.6e-06	1918.280
Science	All	1.0049	-0.000916	-0.000143	2003.788
Single	All	1.0030	-0.000903	+4.5e-06	(2108.349)
Linear plus break fits (Equation 10)					
Dataset	Interval	Constant ($R_0^{(b)}$)	Linear ($R_1^{(b)}$)	Break (T_b)	
Science	Pre-conjunction	1.0121	-0.002774	2010.586	
Single	Pre-conjunction	1.0127	-0.003342	2010.830	
Science	All	1.0154	-0.003542	2010.760	
Single	All	1.0029	-0.000852	2008.0130	

the pre-conjunction data lie very close together, i.e. the contribution of the quadratic term is negligible. The linear fits show a somewhat steeper degradation rate than the published trend (Tappin, Eyles, and Davies, 2015); however, even when extrapolated to 2022, the differences are less than 0.5%.

The linear fits with a break appear to be decidedly anomalous, as they give a far steeper degradation rate after the break than the linear and quadratic fits. The most likely explanation is that the model is not a good match to the dataset for HI-2A. It is also very clear that although the linear and quadratic pre-conjunction fits match each other very well, none of them line up with the post-conjunction fit.

In Figure 12, we show all of the relevant fits to the single-exposure data (the quadratic fit is not included as, similarly to the pre-conjunction fits, it is almost indistinguishable from the linear fit). As with HI-1A, it is clear that the currently-used fit does not extrapolate well to the post-conjunction interval. However, in this case none of the fits to all of the data agree well with the fits to the two intervals separately. It therefore appears that the best option for HI-2A is to use two independent linear fits, one for the pre-conjunction observations and one for the post-conjunction observations.

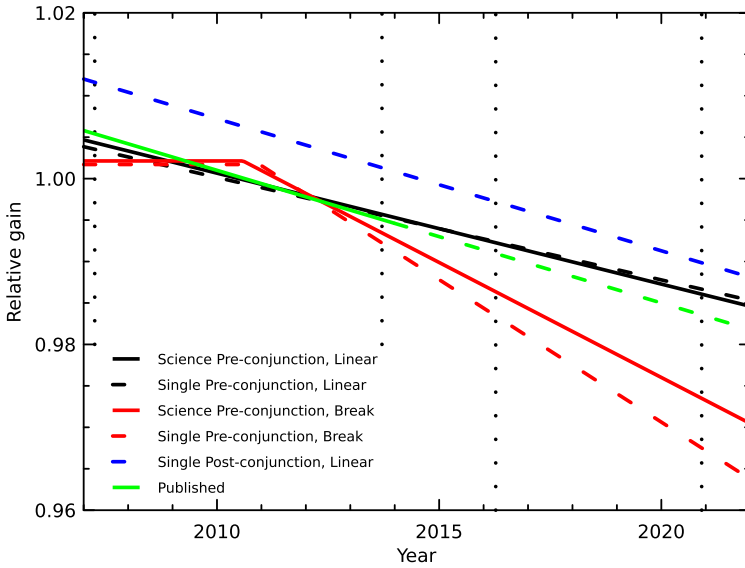


Figure 11 Comparison of the linear and linear-with-break fits to the pre-conjunction HI-2A data (the quadratic ones are omitted as these lie very close to the linear fits). In addition, the published fit from Tappin, Eyles, and Davies (2015) and a linear fit to the single-exposure post-conjunction data are included. The vertical dotted lines delimit the fitting intervals.

5. Synthesis

To produce a revised set of calibration parameters, we must combine the overall levels obtained from the pre-conjunction science data with the trends from the single-exposure data for the entire mission.

Since the trend fits were generated using data normalized over the pre-conjunction interval, we expect that the fitted functions should have a mean value of 1.0 over that interval. Since this is also the interval used to determine the overall level, the gain variation is simply the product of the two components.

5.1. HI-1A

For HI-1A, the trend is best approximated by Equation 10, and the average value between two times (T_1 and T_2) assumed to span the break at T_b is given by:

$$R_{avg}^{(b)}(T_1 : T_2) = \frac{(R_0^{(b)} + R_1^{(b)} T_b)(T_b - T_1) + \left(R_0^{(b)} + R_1^{(b)} \frac{T_b + T_2}{2}\right)(T_2 - T_b)}{T_2 - T_1}, \tag{11}$$

where the times are in years after 2007.0. Putting in the numbers (from the final row of Table 7):

$$\begin{aligned} R_0^{(b)} &= 1.0078, \\ R_1^{(b)} &= -0.001736 \\ T_b &= 2011.486 - 2007.0 = 4.486 \\ T_1 &= 2007.25 - 2007.0 = 0.25 \quad (2007, \text{ day } 91) \\ T_2 &= 2013.72 - 2007.0 = 6.72 \quad (2013 \text{ day } 260) \end{aligned}$$

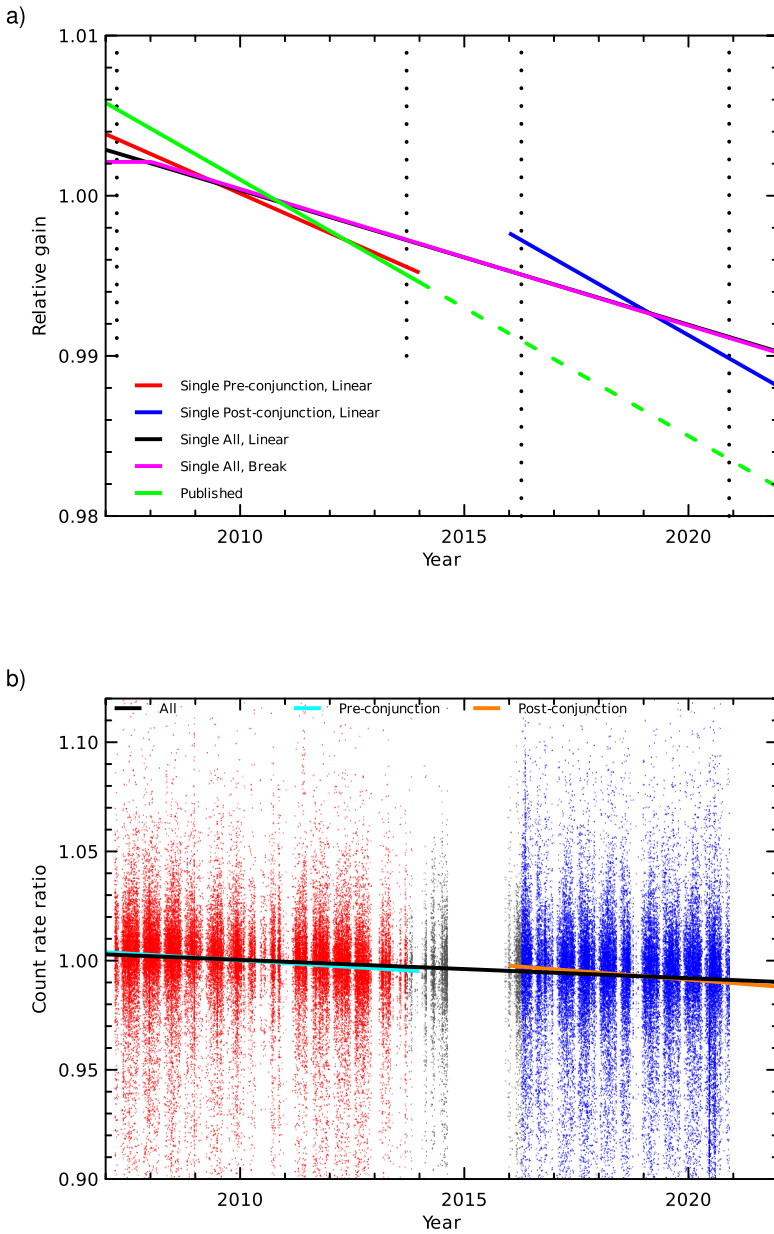
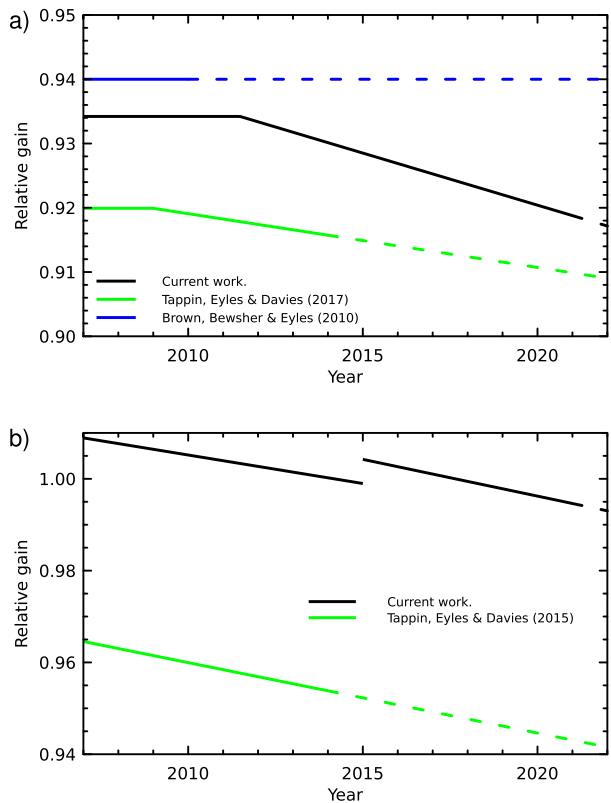


Figure 12 (a) Summary of fits to single-exposure data for HI-2A. (b) The linear fits overlaid on the individual measurements. In (b) the red points are the pre-conjunction interval, blue the post-conjunction interval, and grey the conjunction interval which was not used in the fitting. The linear fits to the pre- and post-conjunction data are also shown as cyan and orange traces, respectively, to contrast with the individual data points. N.B. The y-axis scale in both panels has a smaller range than in the corresponding panels in Figure 10.

we get, $R_{\text{avg}}^{(b)}(T_1 : T_2) = 0.9993$, which is not significantly different from 1.0. Hence, combining with the pre-conjunction median of the science data from Table 4 (row 1) we arrive

Figure 13 Comparison of the determinations STEREO-A HI instrument gains as a function of time: (a) HI-1A, (b) HI-2A. The dashed regions are beyond the data in the determinations. Gains are relative to the pre-launch modelling.



at an adjustment to the pre-launch gain determination of:

$$G_{HI-1A}(T) = 0.9342 \times (1.0078 - 0.001736 (\max(T, 2011.486) - 2007)) \tag{12}$$

$$= 0.9415 - 0.001622(\max(T, 2011.486) - 2007),$$

this gives a sensitivity between the previous determinations of Bewsher et al. (2010) and of Tappin, Eyles, and Davies (2017) as shown in Figure 13a.

5.2. HI-2A

For HI-2A, we need to use two separate linear fits to adequately fit the trends in the single-exposure data for the whole mission, namely the second and fourth lines of Table 8, i.e.:

$$R(T) = \begin{cases} 1.0039 - 0.001236 (T - 2007) & \text{when } T < 2015 \\ 1.0120 - 0.001594 (T - 2007) & \text{when } T \geq 2015 \end{cases} \tag{13}$$

which averages to 0.9996 over the pre-conjunction interval, again close enough to 1.0. So, combining with the pre-conjunction median gain of the science data from the first row of

Table 6 we get an adjustment to the pre-launch gain of:

$$\begin{aligned}
 G_{\text{HI-2A}}(T) &= 1.005 \times \begin{cases} 1.0039 - 0.001236(T - 2007) & \text{when } T < 2015 \\ 1.0120 - 0.001594(T - 2007) & \text{when } T \geq 2015 \end{cases} \\
 &= \begin{cases} 1.0089 - 0.001242(T - 2007) & \text{when } T < 2015 \\ 1.0171 - 0.001602(T - 2007) & \text{when } T \geq 2015 \end{cases}
 \end{aligned} \quad (14)$$

This result is about 4–5% more sensitive than we determined in Tappin, Eyles, and Davies (2015) (Figure 13b).

5.3. Physical Units

The conversions to physical units follow the same logic as presented in Tappin, Eyles, and Davies (2015, 2017), giving conversion factors as:

$$\begin{aligned}
 C(B_{\odot}) &= \frac{n_{\text{pix}}}{I_{\odot}}, \\
 C(S10) &= \frac{1}{I_{10}\Omega_{\text{deg}}}, \\
 C(SI) &= \frac{P}{I_{\odot}\Omega_{\text{pix}}},
 \end{aligned} \quad (15)$$

where n_{pix} is the number of pixels covered by the solar image, I_{\odot} is the computed total counting rate in DN s^{-1} , I_{10} is the computed count rate for a magnitude 10 solar-type star, Ω_{deg} is the solid angle subtended by a pixel, in square degrees, Ω_{pix} is the solid angle subtended by a pixel, in steradians, and P is the total power in the solar spectrum.

As was done by Tappin, Eyles, and Davies (2015, 2017) we have used the solar spectrum of Neckel and Labs (1984), and the total solar irradiance from Kopp and Lean (2011) as the basis for our conversions. The resulting on-axis conversion factors are tabulated in Table 9. The off-axis adjustment is discussed in the previous calibration analyses, i.e. Tappin, Eyles, and Davies (2017) for HI-1 and Tappin, Eyles, and Davies (2015) for HI-2.

6. Discussion

Although the analysis described in this article is couched in terms of ‘pre-conjunction’ and ‘post-conjunction’ data, the true discriminator is the pointing control process. Up to 17 September 2013 (day 260), the pointing control loop of the STEREO-A spacecraft used the gyros to optimise the short-term pointing stability, thereafter, the pointing control loop was closed around the guide telescope and the Sun sensors. This resulted in a considerable degradation of pointing on the timescale of minutes that in turn led to the flagging of some pixels in star images as particle hits. Since this is a consequence of the large spatial gradients in stellar images being converted to temporal changes of signal in individual pixels, the response to heliospheric structures is unaffected, but calibration using stellar photometry on the science images is no longer feasible.

Fortunately, the (approximately) daily single exposure images taken by the HI cameras do not have particle scrubbing applied and so they can be used for calibration purposes. By comparing the single-exposure data with the science data, it was clear that despite the much shorter total integration of the single-exposure images the two datasets gave consistent results for the pre-conjunction interval. This has allowed us to extend the calibration determination up to the present time.

We have found that the low degradation rates (less than 0.2% per year) of both HI instruments have continued with no significant acceleration. If this continues into the future,

Table 9 On-axis conversion factors from count rates ($\text{DN s}^{-1} \text{ CCD pixel}^{-1}$) to physical units for the STEREO-A HI instruments.

HI-1A			
Unit	Constant	Linear	Break
	$(R_0^{(b)})$	$(R_1^{(b)})$	(T_b)
B_{\odot}	3.435E-13	-5.914E-16	2011.486
S10	763.2	-1.315	2011.486
$\text{W m}^{-2} \text{ sr}^{-1} (0-\infty)$	6.867E-06	-1.183E-08	2011.486
$\text{W m}^{-2} \text{ sr}^{-1} (360-1800 \text{ nm})$	4.894E-06	-8.429E-09	2011.486
$\text{W m}^{-2} \text{ sr}^{-1} (\text{Passband})$	7.767E-07	-1.338E-09	2011.486
HI-2A before 2015.0			
Unit	Constant	Linear	
	(R_0)	(R_1)	
B_{\odot}	4.476E-14	-5.511E-17	
S10	99.50	-0.1225	
$\text{W m}^{-2} \text{ sr}^{-1} (0-\infty)$	8.952E-07	-1.102E-09	
$\text{W m}^{-2} \text{ sr}^{-1} (360-1800 \text{ nm})$	6.218E-07	-7.656E-10	
$\text{W m}^{-2} \text{ sr}^{-1} (\text{Passband})$	3.318E-07	-4.085E-10	
HI-2A after 2015.0			
Unit	Constant	Linear	
B_{\odot}	4.512E-14	-7.107E-17	
S10	100.3	-0.1580	
$\text{W m}^{-2} \text{ sr}^{-1} (0-\infty)$	9.024E-07	-1.421E-09	
$\text{W m}^{-2} \text{ sr}^{-1} (360-1800 \text{ nm})$	6.268E-07	-9.873E-10	
$\text{W m}^{-2} \text{ sr}^{-1} (\text{Passband})$	3.345E-07	-5.269E-10	

it is highly unlikely that the lifetime of the HI instruments will be limited by instrumental degradation. Continuing re-evaluation of the instrument performance every few years will be advisable to monitor any degradation.

For astrophotometry, the pointing degradation does limit the possibilities with the science data. While major outbursts will still be seen, precise photometry will likely be limited to the single-exposure data and to special campaigns, such as the ongoing observations of Betelgeuse with HI-2A (Dupree et al., 2020).

We have not attempted to update the large scale flat fields as there is no reason to expect these to change, and the more sparse data of the single-exposure data would add little in terms of improvement to the signal-to-noise ratio.

7. Summary

- i) The HI instruments on STEREO-A continue to perform very well, with less than 0.2% per year loss of photometric sensitivity.
- ii) The pointing degradation following the turning-off of the gyros means that the science data can no longer be used for calibration (or for high-precision astrophotometry).

Table 10 Median gains for HI-2B using the methods described for HI-2A.

Sample	N_{stars}	Simple median		Constrained fit	
		Gain	Error	Gain	Error
Science	253	1.056	0.025	1.070	0.04
Science ($m_v < 6$, $R = 100$)	42	1.079	0.03	1.080	0.07
Tappin, Eyles, and Davies (2015)	54			1.057	0.03

- iii) The single-exposure images provide sufficient precision to allow the monitoring of the evolution of the photometric sensitivity of the instrument.
- iv) The revisions to the calibration parameters will be incorporated into the SolarSoft suite (Freeland and Handy, 1998).

Appendix 1: HI-2B Check

In view of the fairly significant changes required to the HI-2A photometric calibration, we consider it necessary to verify whether the methods used in the current analysis also imply changes to the photometric calibration of HI-2B.

Since there was only a short interval between the turn-off of the gyros on STEREO-B on 7 January 2014 (day 7) and the loss of communication on 1 October 2014 (day 274), there is no need to make use of data from gyroless operations and hence no need to use the single-exposure data.

We have used the same base sample and selection criteria as described in Section 3.2.1 and Table 5. Although the criteria are the same, the star list does differ, in particular only 253 stars passed (c.f. 448 for HI-2A), primarily because of poor positional correlations resulting from the larger point spread function of HI-2B. We also analysed the most restricted set of criteria (stars brighter than $m_v = 6.0$ and using only the inner 100 bins). The results are summarized in Table 10. As can be seen, the sensitivities derived using the updated methods match those of Tappin, Eyles, and Davies (2015) to well within the error limits.

Similarly, we followed the analysis of Sections 4.1 and 4.3 to determine a degradation rate for HI-2B. For the main sample and the bright sample in the inner 100 bins, we found a degradation of 0.1% per year, compared with 0.07% per year in Tappin, Eyles, and Davies (2015).

Based on this, we do not consider it necessary to make any updates to the parameters for HI-2B published by Tappin, Eyles, and Davies (2015), as the differences lie well within the error limits.

Acknowledgments The Heliospheric Imager (HI) instrument was developed by a collaboration that included the Rutherford Appleton Laboratory and the University of Birmingham, both in the United Kingdom, and the Centre Spatial de Liège (CSL), Belgium, and the US Naval Research Laboratory (NRL), Washington DC, USA. The STEREO/SECCHI project is an international consortium of the Naval Research Laboratory (USA), Lockheed Martin Solar and Astrophysics Lab (USA), NASA Goddard Space Flight Center (USA), Rutherford Appleton Laboratory (UK), University of Birmingham (UK), Max-Planck-Institut für Sonnensystemforschung (Germany), Centre Spatial de Liège (Belgium), Institut d'Optique Théorique et Appliquée (France), and Institut d'Astrophysique Spatiale (France).

Data Availability All STEREO-HI data are available for download from the UK Solar System Data Centre (UKSSDC; <https://www.ukssdc.ac.uk/solar/stereo/>). Free registration is required.

Declarations

Disclosure of Potential Conflicts of Interest The authors declare that they have no conflicts of interest.

Open Access This article is licensed under a Creative Commons Attribution 4.0 International License, which permits use, sharing, adaptation, distribution and reproduction in any medium or format, as long as you give appropriate credit to the original author(s) and the source, provide a link to the Creative Commons licence, and indicate if changes were made. The images or other third party material in this article are included in the article's Creative Commons licence, unless indicated otherwise in a credit line to the material. If material is not included in the article's Creative Commons licence and your intended use is not permitted by statutory regulation or exceeds the permitted use, you will need to obtain permission directly from the copyright holder. To view a copy of this licence, visit <http://creativecommons.org/licenses/by/4.0/>.

References

- Bewsher, D., Brown, D.S., Eyles, C.J.: 2012, Long-term evolution of the photometric calibration of the STEREO Heliospheric Imagers: I. HI-1. *Solar Phys.* **276**(1–2), 491. [DOI](#). [ADS](#).
- Bewsher, D., Brown, D.S., Eyles, C.J., Kellett, B.J., White, G.J., Swinyard, B.: 2010, Determination of the photometric calibration and large-scale flatfield of the STEREO Heliospheric Imagers: I. HI-1. *Solar Phys.* **264**(2), 433. [DOI](#). [ADS](#).
- Dupree, A., Guinan, E., Thompson, W.T., STEREO/SECCHI/HI Consortium: 2020, Photometry of betelgeuse with the STEREO mission while in the glare of the Sun from Earth. *Astron. Telegram* **13901**, 1. [ADS](#).
- Eyles, C.J., Harrison, R.A., Davis, C.J., Waltham, N.R., Shaughnessy, B.M., Mapson-Menard, H.C.A., Bewsher, D., Crothers, S.R., Davies, J.A., Simnett, G.M., Howard, R.A., Moses, J.D., Newmark, J.S., Socker, D.G., Halain, J.-P., Defise, J.-M., Mazy, E., Rochus, P.: 2009, The Heliospheric Imagers onboard the STEREO mission. *Solar Phys.* **254**(2), 387. [DOI](#). [ADS](#).
- Freeland, S.L., Handy, B.N.: 1998, Data analysis with the SolarSoft system. *Solar Phys.* **182**(2), 497. [DOI](#). [ADS](#).
- Hoffleit, D., Warren, W.H. Jr.: 1995, VizieR Online Data Catalog: Bright Star Catalogue, 5th revised ed. (Hoffleit+, 1991). *VizieR Online Data Catalog*, V/50. [ADS](#).
- Howard, R.A., Moses, J.D., Vourlidas, A., Newmark, J.S., Socker, D.G., Plunkett, S.P., Korendyke, C.M., Cook, J.W., Hurley, A., Davila, J.M., Thompson, W.T., St Cyr, O.C., Mentzell, E., Mehalick, K., Lemen, J.R., Wuelser, J.P., Duncan, D.W., Tarbell, T.D., Wolfson, C.J., Moore, A., Harrison, R.A., Waltham, N.R., Lang, J., Davis, C.J., Eyles, C.J., Mapson-Menard, H., Simnett, G.M., Halain, J.P., Defise, J.M., Mazy, E., Rochus, P., Mercier, R., Ravet, M.F., Delmotte, F., Auchere, F., Delaboudiniere, J.P., Bothmer, V., Deutsch, W., Wang, D., Rich, N., Cooper, S., Stephens, V., Maahs, G., Baugh, R., McMullin, D., Carter, T.: 2008, Sun Earth Connection Coronal and Heliospheric Investigation (SECCHI). *Space Sci. Rev.* **136**(1–4), 67. [DOI](#). [ADS](#).
- Kaiser, M.L., Kucera, T.A., Davila, J.M., St. Cyr, O.C., Guhathakurta, M., Christian, E.: 2008, The STEREO mission: an introduction. *Space Sci. Rev.* **136**(1–4), 5. [DOI](#). [ADS](#).
- Koenker, R., Hallock, K.F.: 2001, Quantile regression. *J. Econ. Perspect.* **15**, 143.
- Kopp, G., Lean, J.L.: 2011, A new, lower value of total solar irradiance: evidence and climate significance. *Geophys. Res. Lett.* **38**(1), L01706. [DOI](#). [ADS](#).
- Myers, J.R., Sande, C.B., Miller, A.C., Warren, W.H. Jr., Tracewell, D.A.: 2001, VizieR Online Data Catalog: SKY2000 Catalog, Version 4 (Myers+ 2002). *VizieR Online Data Catalog*, V/109. [ADS](#).
- Neckel, H., Labs, D.: 1984, The solar radiation between 3300 and 12500 Å. *Solar Phys.* **90**(2), 205. [DOI](#). [ADS](#).
- Pickles, A.J.: 1998a, A stellar spectral flux library: 1150–25 000 Å. *Publ. Astron. Soc. Pac.* **110**(749), 863. [DOI](#). [ADS](#).
- Pickles, A.J.: 1998b, VizieR Online Data Catalog: A Stellar Spectral Flux Library: 1150–25 000 Å (Pickles 1998). *VizieR Online Data Catalog*, J/Publ. Astron. Soc. Pac./110/863. [ADS](#).
- Tappin, S.J.: 2017, Considerations for the use of STEREO-HI data for astronomical studies. *Astron. J.* **153**(4), 164. [DOI](#). [ADS](#).
- Tappin, S.J., Eyles, C.J., Davies, J.A.: 2015, Determination of the photometric calibration and large-scale flatfield of the STEREO Heliospheric Imagers: II. HI-2. *Solar Phys.* **290**(7), 2143. [DOI](#). [ADS](#).
- Tappin, S.J., Eyles, C.J., Davies, J.A.: 2017, On the long-term evolution of the sensitivity of the STEREO HI-1 cameras. *Solar Phys.* **292**(2), 28. [DOI](#). [ADS](#).

Publisher's Note Springer Nature remains neutral with regard to jurisdictional claims in published maps and institutional affiliations.